AUTOMATYKA • 2010 • Tom 14 • Zeszyt 3/2

Kostadin Brandisky*, Andrzej Romanowski**,
Krzysztof Grudzień**, Dominik Sankowski**

Electrostatic Field Simulations in the Analysis and Design of Electrical Capacitance Tomography Sensors

1. Introduction

Electrical Capacitance Tomography (ECT) is used in many industrial processes for visualizations and determination of flow parameters. It consists in measurement of the mutual capacitances between electrodes of a sensor placed around the flow pipe, and solving the inverse problem of finding the permittivity distribution, minimizing the difference between the measured and computed capacitances.

One of the main tasks in application of ECT is to compute the capacitances between the electrodes at specified distribution of the permittivity of the dielectric materials and calculation sensor sensitivities maps. This is done usually by numerical methods, mostly using the Finite Element Method (FEM), but also using Boundary Element Method (BEM), statistical Monte Carlo integration, method of moments, fast multipole methods, etc.

While many papers exist on the ECT systems, their hardware and inverse algorithm solution, comparatively few papers have been published considering the numerical simulation of ECT sensors from the point of view of improving their design.

From the reviewed papers in the last several years, the following topics relating the electrostatic field computations with the effective sensor design can be found:

- Investigating the influence of the number and length of the electrodes on the inter-electrode capacitances and on the image resolution [10, 11].
- Investigating the influence of axial end screens on the spatial resolution and active sensing area [1, 2, 3, 9].
- Investigating the influence of the inter-electrode shields (strips or bars) [1].
- Investigating the influence of the outer shield [11].
- Investigating the influence of the pipe wall thickness and permittivity [10].

* Technical University of Sofia, Bulgaria
** Computer Engineering Department, Technical University of Lodz, Poland

- Investigating the influence of the shift between the layers of electrodes [6].
- Investigating the effect of the active guard electrodes [1, 2, 11].
- Investigating the difference between 2D and 3D analysis of sensors[1, 8].
- Investigating the measurement protocols used on the image resolution [5].
- Investigating the influence of the different electrode shapes on the image resolution [6, 7].

The main use of the electrostatic field analysis in ECT process can be summarized as:

- To solve the forward problem and to compute the capacitance matrices for the inverse problem solution, with possibility to change the permittivities of the volume cells between the iterations.
- To compute the sensitivity matrices for use in the inverse solution and for improving their uniformity by varying different parameters for better electrode design.
- To simulate the whole inverse problem solution for training purposes, without using measured capacitances.

It can be concluded, that most of the papers consider the difference between 2D and 3D analysis, the length of the electrodes, the effects of the shields and the guards on the sensitivity. Comparatively small number of papers considers and comments different shapes of electrodes, here must be mentioned [6, 7]. They mostly give general recommendations and analyze and discuss some results of different electrode shapes. This is an open field of investigation where FEM modelling and analysis can help.

The analysis of the electrostatic field in ECT sensors and the computation of capacitances and sensitivities are of key importance for the 3D analysis of electrical field, but also crucial to even 2D ECT. Their efficient computation is very important, especially when 3D analysis is performed. The parallelization of these computations can speed-up the whole ECT process.

2. Electrostatic field

The electrostatic field is called the field created by static charged particles, which charges are constant in time. Its equations can be derived from the full Maxwell system of equations for motionless media, when $\partial\mathbf{B}/\partial t = 0$ and $\partial\mathbf{D}/\partial t = 0$ are substituted, because of the static character of the field [14]. Besides, currents are not present because the charged particles are immobile, and thus $\mathbf{J} = 0$.

The only sources of the electrostatic field are the charges of the charged particles. In this case there is no connection between the electric and magnetic quantities and thus, the electrostatic and the magnetostatic fields can be analyzed independently.

Thus, simplifying the full system Maxwell equations, the equations of the electrostatic field will be:

$$\operatorname{rot}\mathbf{E} = 0 \tag{1}$$

$$\operatorname{div}\mathbf{D} = \rho \tag{2}$$

$$\mathbf{D} = \varepsilon\mathbf{E} \tag{3}$$

where:

E – electric field intensity,
D – electric flux density,
ε – permittivity of the medium,
ρ – charge density.

The equation $\operatorname{rot}\mathbf{E} = 0$ shows, that the electrostatic field is a potential field. For potential fields, a scalar function $V(x, y, z)$ can be introduced, called *electric potential*. It is defined as:

$$\mathbf{E} = -\operatorname{grad} V \tag{4}$$

because Eq. (4) satisfies the equation $\operatorname{rot}\mathbf{E} = 0$, as the vector identity $\operatorname{rot}\operatorname{grad}V = 0$ holds true.

It is known from the mathematical physics, that the solution of the Eqs. (1)–(3) is not unique. These equations are supplemented by boundary conditions for the quantities electric flux density **D** and electric field intensity **E** on the interface between two media having different electrical properties. Using these boundary conditions, a unique solution of the electrostatic field equations can be found. The general form of the boundary condition, when there are no static charges at the interface, is

$$\frac{\tan\theta_1}{\tan\theta_2} = \frac{\varepsilon_1}{\varepsilon_2} \tag{5}$$

Here, θ_1 and θ_2 are the angles between the vectors $\mathbf{E_1}$ and $\mathbf{E_2}$ and the normal to the interface between two dielectrics with different permittivities, ε_1 and ε_2.

The main task of the Electrostatics is to find the distribution of the electric potential V and the electric intensity **E** in every point of the field, given the charges or potentials of the charged bodies. Using the voltage or electric field intensity distribution, the picture of the electrostatic field can be plotted. Also, integral quantities like capacitances, energies or forces can be determined, which is important practical task.

In the electrostatic problems, if the charges are confined to the surfaces of conductors and insulators, so that there is no free charge within the volume of a material, the equation (2) reduces to:

$$\operatorname{div}\mathbf{D} = 0 \tag{6}$$

To solve this equation, we first replace **D** using Eq. (3), and then replace **E** using Eq. (4). Eq. (6) then becomes

$$\operatorname{div}\left(\varepsilon \operatorname{grad} V\right) = 0 \tag{7}$$

which can be solved numerically using the Finite Element Method to determine the electric field in the device.

The Eq. (2) has integral form, called Gauss's Law

$$\oiint_{(S)} \mathbf{D}\,\mathbf{ds} = q \tag{8}$$

where q is the charge of the particles, existing in the volume with outer area S. It is often used to calculate the charges and then – the capacitances of ECT sensors. The integral in Eq. (8) can be solved analytically for regions that have symmetry. In other cases, the integration has to be done numerically.

There are many methods to solve the main electrostatic equation (7), but the most widely use has found the Finite Element Method (FEM). In the FEM, the region under analysis is subdivided to elementary subregions, called elements, which in most of the cases are triangles (for 2D problems) or tetrahedra (for 3D problems). The unknown distribution of the potential is approximated by simple polynomials inside the elements, and the nodal values of the potential are taken as unknowns. For every element local matrices are built using this polynomial representation, and then the local matrices are assembled in one global matrix, valid for the whole region. The unknowns in this matrix are the nodal values of the potentials in the region. Solving the system, which is linear when linear materials are used, or non-linear, when non-linear materials are used, will give the unknown potential distribution. Using the potentials in the nodes, the electric field intensities can be found in every element, and then, many global quantities like charges on the electrodes, capacitances, electric energy, power, forces between electrodes, etc., can be found. Increasing the number of nodes in the region, allows more accurate solution of the problem to be found, as the approximated potential distribution will be more close to the real distribution.

3. Capacitance values determination

The capacitance is an integral characteristic of a capacitor, which is defined by the ratio of the absolute value of the charge on one of the electrodes to the absolute value of the potential difference between the electrodes of a capacitor (Eq. (9)):

$$C = \frac{q}{u} = \frac{q}{V_1 - V_2} \tag{9}$$

Using the electrostatic field quantities and Eq. (8), the capacitance can be defined also as (Eq. (10)):

$$C = \frac{\oiint_{S} \varepsilon\,\mathbf{E}\,\mathbf{ds}}{\int_{1}^{2} \mathbf{E}\,\mathbf{dl}} \tag{10}$$

The capacitance does not depend on the voltage or on the charge, because their ratio is a constant. The capacitance is a function only of the physical dimensions of the system and the permittivities of the dielectric materials. Common way for determining the capacitance of a capacitor is to apply Eq. (10), computing the charge and the voltage between the plates using the electric field intensity. Alternatively, the capacitance may be calculated from the stored electric energy:

$$W_e = \frac{1}{2} C u^2 \rightarrow C = \frac{2W_e}{u^2} \tag{11}$$

The self capacitance of an electrode can be obtained by exciting this electrode with known voltage, e.g., 1 V, leaving all other electrodes to zero potential, and computing the stored electric energy. The stored electric energy can be computed by integration, element by element if the FEM is used, using the computed electric potentials in the nodes

$$W_e = \frac{1}{2} \iiint_{(v)} \mathbf{D} \cdot \mathbf{E} \, dv = \frac{1}{2} \iiint_{(v)} \varepsilon \mathrm{E}^2 dv = \frac{1}{2} \iiint_{(v)} \varepsilon \left(grad \, \mathrm{V} \right)^2 dv \tag{12}$$

Every electromagnetic CAD system has a built-in function which computes the stored electric energy. If a system having more than two charged bodies is considered, the partial capacitances between each couple of electrodes must be defined. As a whole, the capacitance matrix of *n*-electrode sensor is given as:

$$C = \begin{bmatrix} C_{11} & C_{12} & \cdots & C_{1n} \\ C_{21} & C_{22} & \cdots & C_{2n} \\ \cdots & \cdots & \cdots & \cdots \\ C_{n1} & C_{n2} & \cdots & C_{nn} \end{bmatrix} \tag{13}$$

For the ECT, only the mutual capacitances are necessary, as they are compared with measured capacitances between every two electrodes. Taking in mind that $C_{ij} = C_{ji}$, for *n*-electrode sensor, the number of the mutual capacitances is $N = n(n–1)/2$. From the finite element solution, the easiest way is to find the charges of the electrodes and then to find the ground capacitances, with respect to the ground electrode, using $C = q/u$. The ground capacitances are related to the electrode charges as follows (the equations are for 2-electrode sensor, except the ground):

$$\begin{aligned} q_1 &= C_{11} V_1 + C_{12} V_2 \\ q_2 &= C_{12} V_1 + C_{22} V_2 \end{aligned} \tag{14}$$

These ground capacitances do not represent lumped capacitances typically used in a circuit simulator because they do not relate the capacitances between electrodes. Because

the charges of the non-excited electrodes are negative, the mutual capacitances are negative. Because the charge of the excited electrode is positive, the self capacitance will be positive. From the ground matrix, the lumped capacitance matrix can be derived, which is more useful for the practice, because all mutual capacitances are positive, and can be compared with measured capacitances. The lumped capacitance matrix can be derived in the following way

$$\begin{aligned} q_1 &= \left(C_{11}+C_{12}\right)\left(V_1-0\right)+\left(-C_{12}\right)\left(V_1-V_2\right)=C_{11L}V_1+C_{12L}\left(V_1-V_2\right) \\ q_2 &= \left(-C_{12}\right)\left(V_2-V_1\right)+\left(C_{12}+C_{22}\right)\left(V_2-0\right)=C_{12L}\left(V_2-V_1\right)+C_{22L}V_2 \end{aligned} \tag{15}$$

It is clear that the lumped mutual capacitances can be obtained by reversing the sign of the ground mutual capacitances, and the lumped self capacitances can be obtained by summing all the ground capacitances connected to this electrode.

The energy method for computing the capacitances requires computation of the self and mutual capacitances:

$$C_{ii}=2W_e \quad V_j=\begin{cases} 0 & j\neq i \\ 1 & j=i \end{cases} \tag{16}$$

$$C_{ij}=W_e-\frac{1}{2}\left(C_{ii}+C_{jj}\right) \quad V_k=\begin{cases} 0 & k\neq i,\, j \\ 1 & k=i \\ 1 & k=j \end{cases} \tag{17}$$

Eq. (17) is a consequence from the formula for stored electric energy in a system of coupled capacitors:

$$W_e=\sum_i \frac{C_i V_i^2}{2}+\sum_{i\neq j} C_{ij}\,V_i\,V_j \tag{18}$$

This method requires much more computations, than the charge method, because it includes n computations of the stored energy with only one electrode excited to find the self capacitances C_{ii}, and $n(n-1)/2$ computations of energy, with two electrodes excited, or total of $n(n+1)/2$ computations of energy. For $n = 32$ electrodes in case of 3D ECT sensors this gives $N = 32.33/2 = 528$ computations of the stored energy. Compared with the required number n of FEM computations for the charge method, it is clear that the energy method requires 16.5 times more computations for $n = 32$ electrodes, than the charge method. Of course, this extended time is to some extent compensated with the possible higher accuracy of energy computation, because it integrates over the whole region. In contrast, the charges are computed by the Gauss' law only on the electrode surfaces. It uses the electric field intensity **E**, which values are not so accurate, unless the finite element mesh is very fine. The errors in **E** are more pronounced near sharp corners of electrodes and especially near singularity points, where **E** is practically undefined.

In conclusion, the energy method of capacitance calculation is more accurate but more time-consuming. The calculation of the capacitances of complex two-electrodes or multi-electrode systems is important practical task. Nowadays, it is solved successfully using numerical methods and CAD systems like ElecNet [16], FEMM [15], Comsol [12], etc.

4. Computation of the sensitivity matrices/maps

Sensitivity maps are widely used to evaluate the quality of ECT sensors. Sensitivity map stores information about the change of the capacitance value resulting from the change of permittivity distribution inside the sensor space. The sensitivity $S_{ij}^{(k)}$ in a pixel k of an ECT image represents the change in the capacitance C_{ij} between electrodes i–j caused by a small perturbation in permittivity ε_k of the pixel k.

$$S_{ij}^{(k)} = \frac{\partial C_{ij}}{\partial \varepsilon_k} \tag{19}$$

The set of sensitivities in all pixels of the image for a specific mutual capacitance C_{ij} represents the *sensitivity map* for this capacitance (also called *sensitivity matrix* for this capacitance). The sensitivity in every pixel of the sensitivity map for the pair i–j, is computed by the widely used formula [6, 8]:

$$S_{ij}^{(k)} = -\int_{\Omega_k} \mathbf{E}_i^{(k)} \cdot \mathbf{E}_j^{(k)} \, d\Omega \tag{20}$$

where $\mathbf{E}_i^{(k)}$ is the electric field vector inside the pixel k when the electrode *'i'* is excited with 1 V, $\mathbf{E}_j^{(k)}$ is the electric field vector inside the pixel k when electrode *'j'* is excited with 1 V. The multiplication between the two vectors is a dot product. Ω_k is the area (or the volume of the voxel, in 3D) of the pixel k.

For all excitations the distribution of the potentials is computed by FEM, and then, in the centre of every pixel of the map the vector **E** is found using Eq. (4). The electric field intensity vectors for every case of excitation are stored and then used to compute the sensitivities. The sensitivity matrix **S** is obtained by joining together the sensitivity matrices of all mutual capacitances in a common matrix (Eq. (21)). It is used in the inverse solution methods [17]:

$$\mathbf{S} = \begin{bmatrix} \mathbf{S_{12}} \\ \mathbf{S_{13}} \\ \cdots \\ \mathbf{S_{n-1,n}} \end{bmatrix} \tag{21}$$

Here $\boldsymbol{S_{12}}$ is a vector-row with k elements (k is the number of pixels in the map for sensitivities of the capacitance C_{12}), $\boldsymbol{S_{13}}$ is a vector-row with k elements for sensitivities of the capacitance C_{13}, etc. The number of rows in the sensitivity matrix $\boldsymbol{S}$ is equal to the number of the mutual capacitances $N = n(n-1)/2$. The number of columns of $\boldsymbol{S}$ is equal to k – the number of pixels in the image. Several sensitivity maps for 12-electrodes single layer sensor are shown below as illustrations. Figures 1–4 reveals sensitivity maps for following pairs of electrodes: C_{12}, C_{13}, C_{14} and C_{15}, respectively.

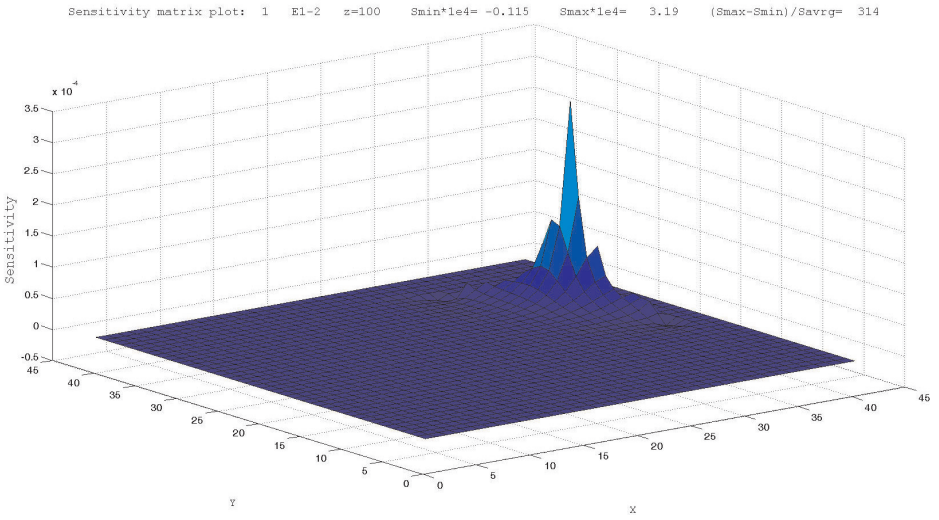

Fig. 1. Sensitivity map for C_{12}

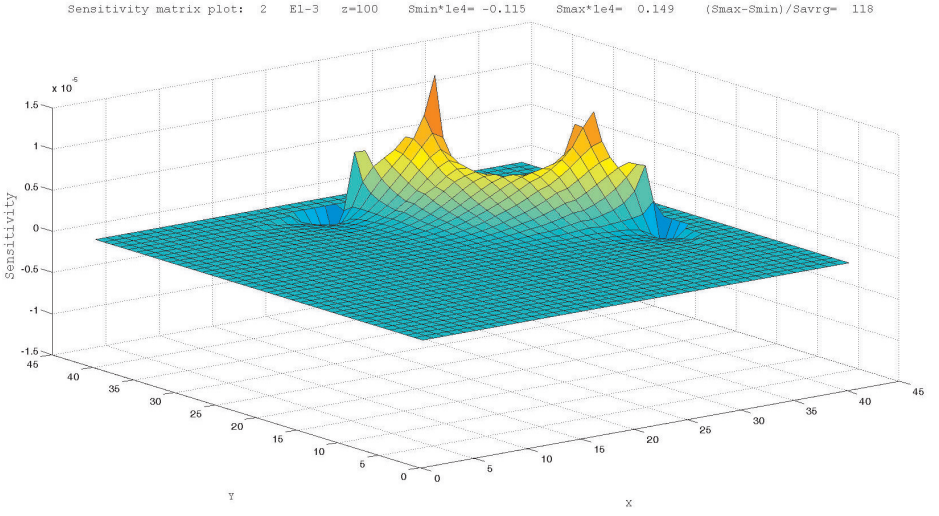

Fig. 2. Sensitivity map for C_{13}

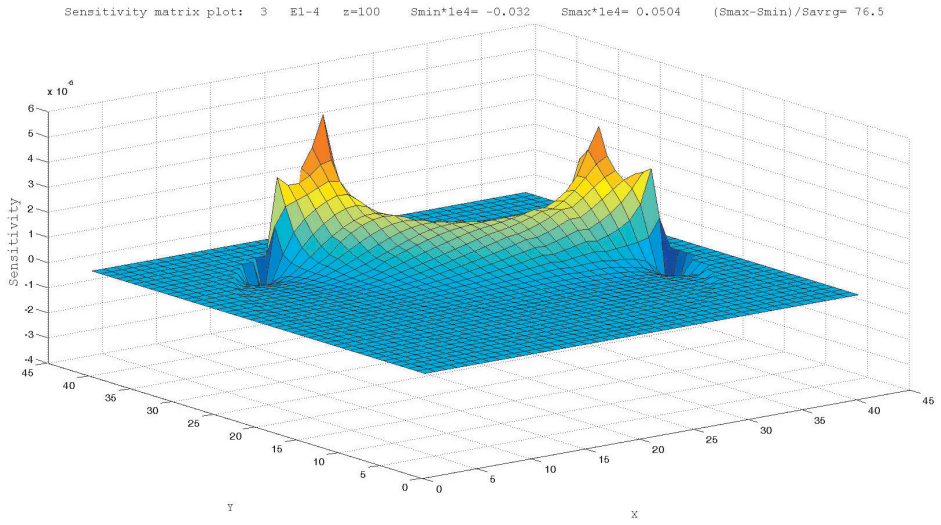

Fig. 3. Sensitivity map for C_{14}

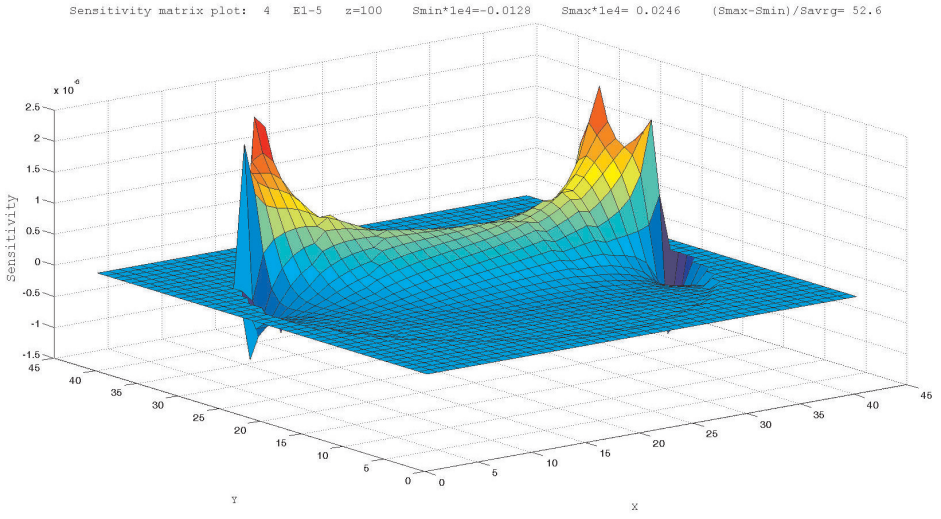

Fig. 4. Sensitivity map for C_{15}

5. Data comparison – gravitational particle flow

In order to compare experimental measurement data and simulation data, a phantom was prepared which was located inside sensor space during the simulation. The local particle concentration is associated with the measured permittivity of the mixed material

(e.g., sand) with air. The more dense packing the greater the value of permittivity in given region. Therefore, the change of *packing density* during discharging of hopper conveys basic information describing the nature of discharge process.

Figure 5 presents, on the left hand side, the cross section of a phantom with 3 different homogeneous regions. Each of these regions had different permittivity value ε_I, ε_{II}, ε_{III}. The so prepared phantom represents real phenomena, which take place during gravitational discharging silo process [18, 19, 20]. Two main regions exist in slim silo flow, viz.: the so-called stagnant zone (located close to the walls of container) and funnel flow (usually present in the centre). These vary only in terms of a slight difference in packing density of material in the two zones. This flow results in the generation of air-filled voids. These small voids or gaps appear among the particles as they process down towards the bottom orifice. The material in the stagnant zone is expected to maintain its packing density fraction; while the material in the dynamic region is less densely packed due to the flow forced by discharging process. General and detailed studies with theoretical models for powder flow are reported in [9, 10].

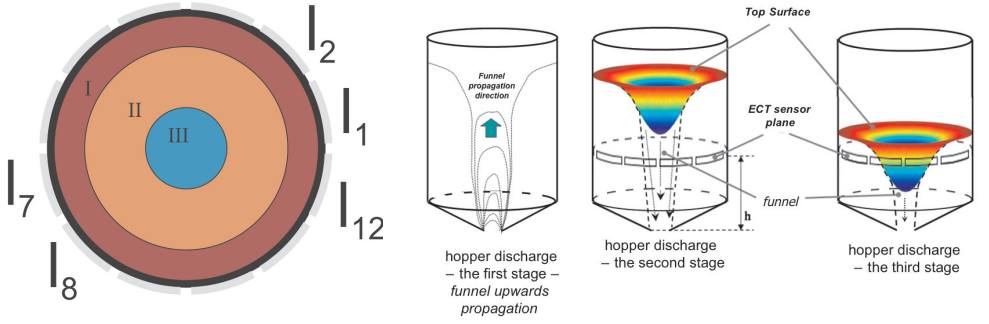

Fig. 5. The LHS presents cross section of prepared phantom (I, II, III means regions with different permittivities ε_I, ε_{II}, ε_{III}), and the last three pictures from the RHS reveal schematically shown hopper discharge stages (funnel propagation, funnel flow, top surface passing through measurement space)

For the purpose of the experiments with ECT the whole process of silo discharging can be split into 3 stages. This partition is presented in form of scheme on the last three right hand side pictures on Figure 5. The first stage starts at the moment of opening the outlet of the container. Then, occurring funnel propagates upwards until reaching the upper surface of the material – this is the point when the first stage is finished and the next one begins. The end of the second stage is dependent on the location of the measurement sensor, since this phase lasts till this sensor zone is reached. The last stage is indicated by the top surface of material passing through sensor zone and the stagnant zone is clearly visible in the measurement space.

The prepared phantom considers the second step of silo discharging, where particle concentration inside the funnel is smaller than that in the stagnant zone. The concentration is indicated through calibrating the measured capacitance with relation to the capacitances

of the full and empty sensor. It can be seen that when the funnel appears, the material situated in stagnant zones by the hopper wall gains a greater packing density – as can be seen from the capacitance time profile for the adjacent electrodes (pair 1–2). On the other hand, capacitance measurements, covering or at least partially including the funnel region, record a decrease. The stagnant zone affects measured capacitance values especially for adjacent electrodes. This validates the behaviour of the examined phenomenon. Figure 6 presents phantom and a model of sensor, both prepared for numerical simulation of electric field during measurements.

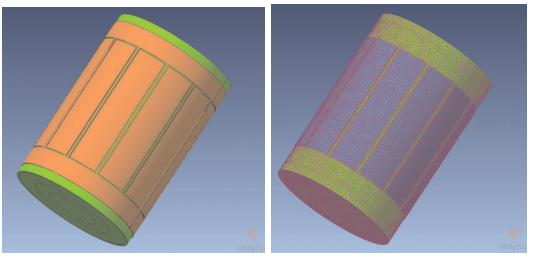

Fig. 6. Phantom model and associated sensor prepared for numerical simulation

In the first step the capacitances were calculated for empty ε_{empty} (for air $\varepsilon_{empty} = 1$) and full ε_{full} (for mixture sand and air $\varepsilon_{full} = 2.5$) sensor. These value are necessary for normalization of the simulated data $\boldsymbol{C}_n$, in the same way as the measurement data. In the first case during simulation the permittivity of regions has values: $\varepsilon'_I = 1.1*\varepsilon_{full}$, $\varepsilon'_{II} = 1.0*\varepsilon_{full}$, $\varepsilon'_{III} = 0.9*\varepsilon_{full}$ and in the second case: $\varepsilon'_I = 1.05*\varepsilon_{full}$, $\varepsilon'_{II} = 1.0*\varepsilon_{full}$, $\varepsilon'_{III} = 0.95*\varepsilon_{full}$. Such changes of the permittivities in these regions were measured in experimental laboratory silo having the same sensor dimensions [21]. The results of the simulated normalisation data with parallel model applied, are presented on Figure 7 for the first case and on Figure 8 for the second case. The presented data show the capacitance changes between the first, and the remaining electrodes $\{C_n^{1-2}, C_n^{1-3}, \ldots, C_n^{1-12}\}$.

The information from the simulation is very helpful to better interpret the measurement data. The big problem during silo monitoring is the lack of knowledge about the real permittivity changes in funnel area or area close to the silo wall based on capacitance measurements changes. The adjacent electrodes capacitances changes of about 10%, compared to the capacitances in the initial stage of the process, can be caused by permittivity value changes of, e.g., 5%. In order to conduct the analysis more accurately, it is necessary to apply series model (Eq. (22)) and Maxwell model (Eq. (23)) to improve the data [22, 23]:

$$C_n^S = \frac{PR * C_n}{1 + C_n * (PR - 1)} \tag{22}$$

$$C_n^M = \frac{C_n * (2 + PR)}{3 + C_n * (PR - 1)} \tag{23}$$

where PR is the permittivity ratio of two materials gas and sand.

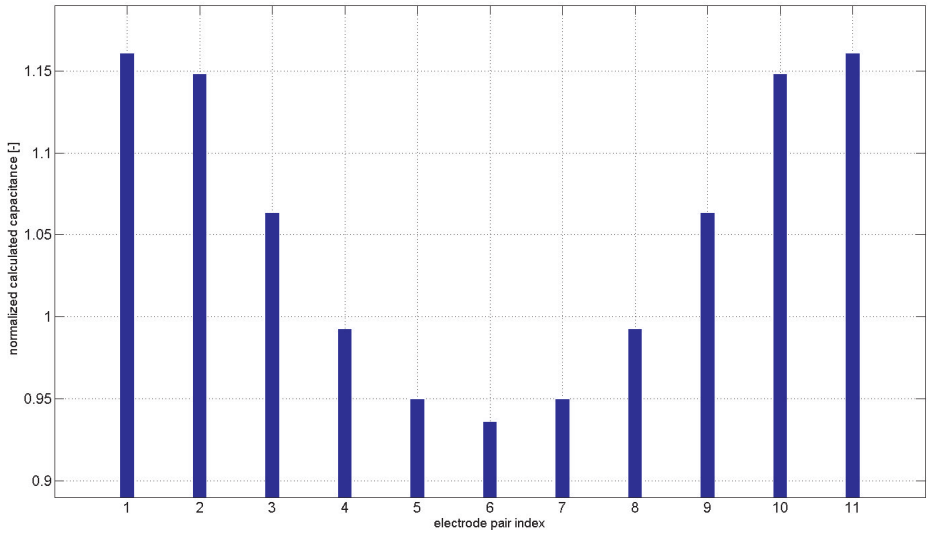

Fig. 7. Simulated normalisation data for phantom of axially symmetrical regions (±10% concentration change): ε'_I=1.1*e_{full}, ε'_{II} =1.0*e_{full}, ε'_{III} = 0.9*e_{full} from Figure 6

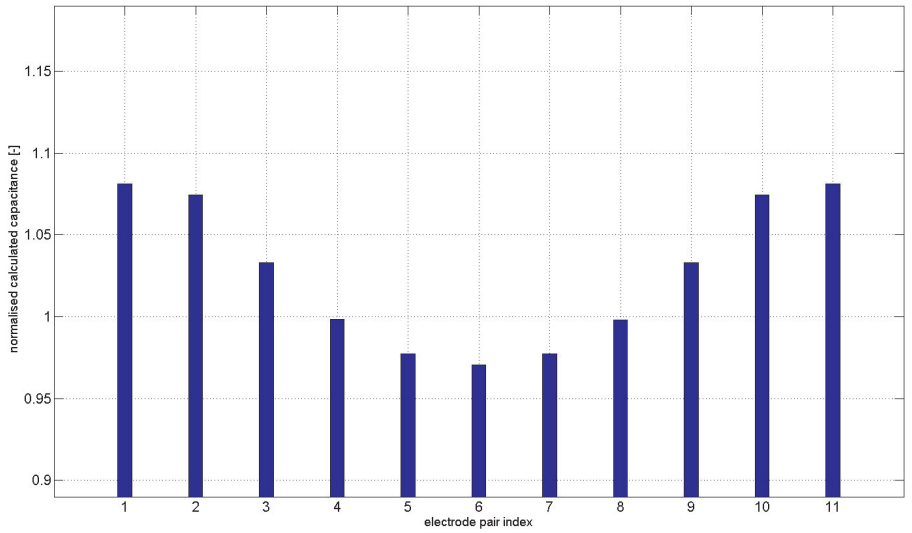

Fig. 8. Simulated normalisation data for phantom of axially symmetrical regions (±5% concentration change): ε'_I=1.05*e_{full}, ε'_{II} =1.0*e_{full}, ε'_{III} = 0.95*e_{full} from Figure 6

Tables 1 and 2 cover normalisation data for different correction of simulation capacitances for 10% and 5% concentration changes (in this case for ±10% and ±5% permittivity changes).

Table 1
Correction results for ±10% concentration change phantom

Type of Correction	C_n^{1-2}	C_n^{1-3}	C_n^{1-4}	C_n^{1-5}	C_n^{1-6}	C_n^{1-7}
Parallel model	1.1608	1.1482	1.0635	0.9929	0.9501	0.9362
Series correction	1.0896	1.0549	1.0245	0.9971	0.9795	0.9736
Maxwell correction	1.1018	1.0942	1.0415	0.9952	0.9661	0.9566

Table 2
Correction results for ±5% concentration change phantom

Type of Correction	C_n^{1-2}	C_n^{1-3}	C_n^{1-4}	C_n^{1-5}	C_n^{1-6}	C_n^{1-7}
Parallel model	1.081	1.0743	1.0329	0.9983	0.9772	0.9705
Series model	1.0309	1.0285	1.0129	0.9993	0.9908	0.988
Maxwell model	1.0526	1.0483	1.0217	0.9988	0.9847	0.9801

6. Conclusions

Application of ECT to measure the slight capacitance changes of bulk materials enables to monitor the processes of storing and discharging of granular materials in real time. One of the characteristic points of the bulk material flow is the dynamic volume changes during the process of receptacle unloading. These changes depend on many factors, such as initial density of the granular material, stress level, mean grain diameter, specimen size and direction of the deformation rate. Additional difficulty lies in the determination of the time-varying factors (humidity, temperature conditions, etc.) influence on the bulk material storage behaviour. Usually it is not easy to forecast such dependences during design stage of the container. Monitoring of granular materials behaviour in silos is crucial for construction site safety. However, the pending problem is to determine the accuracy of dynamic concentration change detection quantitatively, based on both capacitance measurements and reconstructed image. Using raw data, one can only describe the particle concentration change qualitatively. Therefore, the conducted simulation of electrical field inside a model of real tomography sensor allows to approach tuning the ECT system to more accurate concentration change determination for bulk materials. The knowledge of the ECT response caused by changing the concentration of bulk material is the main problem described in the article. Knowledge of the changes of the measurements values caused by a known change in density of bulk material allow to estimate the ECT accuracy. The simulations allow to determine the constant permittivity in the corresponding area of the sensor. Construction of such a real phantom for various values of permittivity is a big problem.

One with possible way to solve this problem is the conducted simulation, which results and comparison them to actual results of the measurements make it possible to better interpret the data measured in actual control systems and industrial process control with the use of ECT.

Presented simulations establish first step of investigation, however already proved its usefulness for ECT performance model validation. The examined case is a very rare example of permittivity distribution change within a narrow range, but changing both within and outside the normalized range. For future work, it seems to be necessary to analyze also the influence of particle material permittivity change within wider range (not only for 5% and 10% concentration changes). The final result will be the information about possibility to scale the normalized measurement values by the coefficient values derived from simulation.

Acknowledgement

The work is funded by the European Community's Sixth Framework Programme – Marie Curie Transfer of Knowledge Action (DENIDIA, contract no: MTKD-CT-2006-039546). The work reflects only the author's views and the European Community is not liable for any use that may be made of the information contained therein.

References

[1] Olmos A.M., Primicia J.A., Marron J.L.F., *Influence of Shielding Arrangement on ECT Sensors*. Sensors, 6, 2006, 1118–1127.

[2] Olmos A.M., Primicia J.A., Marron J.L.F., *Simulation design of electrical capacitance tomography sensors*. IET Sci. Meas. Technol., 1 (4), 2007, 216, 216–223.

[3] Olmos A.M., Carvajal M.A., Morales D.P., Palma A.J., *Influence of design parameters of ECT sensors on the quality of reconstructed images*. Sensors and their Applications XIV (SENSORS07), Journal of Physics: Conference Series, 76, 2007, 012051.

[4] Alme K.J., Mylvaganam S., *Electrical Capacitance Tomography – Sensor Models, Design, Simulations, and Experimental Verification*. IEEE Sensors Journal, vol. 6, No. 5, October 2006.

[5] Alme K.J., Mylvaganam S., *Comparison of Different Measurement Protocols in Electrical Capacitance Tomography Using Simulations*. IEEE Transactions on Instrumentation and Measurement, vol. 56, No. 6, December 2007, 2119.

[6] Warsito W., Marashdeh Q., Fan L.-S., *Electrical Capacitance Volume Tomography*. IEEE Sensors Journal, vol. 7, No. 4, april 2007, 525–535.

[7] Marashdeh Q., Fan L.-S., Du B., Warsito W., *Electrical Capacitance Tomography – A Perspective*. Ind. Eng. Chem. Res., 47, 2008, 3708–3719.

[8] Peng L., Mou C., Yao D., Zhang B., Xiao D., *Determination of the optimal axial length of the electrode in an electrical capacitance tomography sensor*. Flow Measurement and Instrumentation, 16, 2005, 169–175.

[9] Xu H., Yang G., Wang S., *Effect of Axial Guard Electrodes on Sensing Field of Capacitance Tomographic Sensor*. 1st World Congress on Industrial Process Tomography, Buxton, Greater Manchester, April 14–17, 1999, 348–352.

[10] Yang WQ., *Key issues in designing capacitance tomography sensors*. IEEE SENSORS 2006, EXCO, Daegu, Korea, October 22–25, 2006.

[11] Yang WQ., *Design of electrical capacitance tomography sensors*. Meas. Sci. Technol., 21 (2010) 042001 (13pp).
[12] Flores N., Gamio J.C., Ortiz-Aleman C., Damian E., *Sensor Modeling for an Electrical Capacitance Tomography System Applied to Oil Industry*. Proc. of the COMSOL Multiphysics User's Conference, Boston 2005.
[13] Li Y., Yang W.Q., *Virtual electrical capacitance tomography sensor*. Journal of Physics: Conference Series, 15 (2005), 183–188, Sensors & their Applications XIII.
[14] Ida N., *Engineering Electromagnetics*. 2nd ed., Springer-Verlag, New-York, 2003.
[15] Meeker D.C., *Finite Element Method Magnetics*. Version 4.2, available at: http://femm.foster-miller.net (last update 2 Nov 2009) 2010.
[16] Infolytica Corp., ElecNet v. 7.1, 2D & 3D Tutorials, 2010.
[17] Wajman R., Mazurkiewicz Ł., Sankowski D., *The Sensitivity Map in the Image Reconstruction Process for Electrical Capacitance Tomography*. 3rd International Symposium on Process Tomography in Poland, Łódź, 2004.
[18] Grudzien K., Romanowski A., Williams R.A., *Application of a Bayesian approach to the tomographic analysis of hopper flow*. Particle & Particle Systems Characterization, vol. 22, Issue 4, 2005, 246–253.
[19] Romanowski A., Grudzien K., Williams R.A., *Analysis and Interpretation of Hopper Flow Behaviour Using Electrical Capacitance Tomography*. Particle & Particle Systems Characterization, vol. 23, Issue 3–4, 2006, 297–305.
[20] Chaniecki Z., Dyakowski T., Niedostatkiewicz M., Sankowski D., *Application of electrical capacitance tomography for bulk solids flow analysis in silos*. Particle and Particle Systems Characterization, 23, 3–4, 2006, 306–312.
[21] Grudzien K., Romanowski A., Chaniecki Z., Sankowski D., Niedostatkiewicz M., *Description of the silo flow and bulk solid pulsation detection using ECT*. Flow Measurement and Instrumentation, doi:10.1016/j.flowmeasinst.2009.12.006.
[22] Mckeen R., Pugsley T.S., *The influence of permittivity models on phantom images obtained from electrical capacitance tomography*. Meas. Sei. Technol., 13, 2002, 1822–1830.
[23] Process Tomography Ltd. Calculation of volume ratio for ECT sensors. PTL Application Note AN2, 1999, available from: http://www.tomography.com/.